Eur. Phys. J. B (2019) 92: 15
https://doi.org/10.1140/epjb/e2018-90586-5

THE EUROPEAN PHYSICAL JOURNAL B

Regular Article

Effects of orientation and pre-deformation on velocity profiles of dislocation avalanches in gold microcrystals*

Gregory Sparks and Robert Maaß[a]

Department of Materials Science and Engineering and Frederick Seitz Materials Research Laboratory, University of Illinois at Urbana-Champaign, Urbana, IL 61801, USA

Received 3 October 2018 / Received in final form 20 November 2018
Published online 16 January 2019

Abstract. We report on the spatiotemporal dynamics of dislocation avalanches (crystallographic slip) in gold microcrystals with different orientations and also different initial dislocation densities. It is found that the size-integrated averaged velocity profiles have both orientation-dependent and initial-microstructure-dependent peak velocities and velocity decays. With increasing symmetry and apparent strain-hardening rate, the peak velocities decrease and the velocity of the average shape profile decays more slowly with time. These experimental results indicate the material-specific nature of collective dislocation rearrangements that underlie slip events with a net magnitude of a few to several hundred Burgers vectors in the studied microcrystals. Furthermore, we point toward sensitivity to filtering details that may significantly affect conclusions when comparing experiment with theory.

1 Introduction

The evolution of complex systems in response to an external stimulus is a broad topic including many nonequilibrium phenomenon such as earthquakes, snow avalanches, relaxation of glasses, magnetic Barkhausen noise, or the discrete evolution of strain during plastic deformation [1,2]. The latter has a long history, with early observation of discontinuous stress–strain behavior of pure hcp crystals by Becker and Orowan [3], or Tinder and Trzil [4]. These observations stand out, as they highlight the intermittency of plastic flow directly via the observation of extension measurements. Other methods that have indicated the discontinuous evolution of the underlying dislocation structure in a deforming crystal are acoustic emission (AE) measurements [5,6] or time-resolved diffraction [7]. In particular, the AE technique has been employed intensely in the context of crackling noise emitted by metallic materials that exhibit dynamic strain aging [8–11].

While initial AE measurements focused on the relationship between dislocation mechanisms and the characteristics of AE-pulses [12–14], a statistical analysis of pulse energies from creeping ice crystals highlighted the scale-free nature of the underlying plastic fluctuations [5,6]. Such a finding was indeed remarkable, as it suggested that plastic flow is free of scale, which means that the intermittently occurring collective dislocation events lack a well-defined mean of the observed quantity. With the advent of well-controlled small-scale mechanical testing, intermittent flow was routinely observed [15–17] and the scale-freeness derived from AE experiments was confirmed with the direct analysis of strain discontinuities [16,18].

Capturing the scaling properties of plastic strain bursts has since then received considerable attention from the community of nonequilibrium critical phenomena [19–21]. In these works, efforts are dedicated to the interpretation and understanding of how collective dislocation events that mediate crystallographic slip, often referred to as dislocation avalanches, are triggered by the evolving three-dimensional network upon which a far field stress acts as a driving force. The most prominent models that are currently discussed are a mean-field (MF) model [22,23] in which the dislocation system is undergoing a repeated pinning–depinning transition and a model that relies on the evolving network that jams and unjams via sudden collective rearrangements [24–26]. The core of these activities is dedicated to quantifying and predicting how some probability of an event of size S evolves as a function of event size, where some form of power-law scaling $P(S) \propto S^{-\tau}$ is the recurring theme. Attention must be paid to the type of probability distribution when comparing τ with a given theoretical model. In the particular case of MF depinning, $\tau = 1$ for a stress-integrated complementary cumulative distribution function (CCDF), and $\tau = 0.5$ in the case of a stress-binned CCDF [23]. In the case of

* Contribution to the Topical Issue "Complex Systems Science meets Matter and Materials", edited by Stefano Zapperi.

[a] e-mail: rmaass@illinois.edu

jamming–unjamming, τ is not predefined to a given value but is nontrivial and lower than in the case of MF [26].

The aforementioned debate is primarily driven by theory and modeling, whereas our own efforts have attempted to contribute via systematic experimentation so as to scrutinize proposed models [27–33]. Our experiments that trace not only event sizes but also their time-resolved velocity profiles have revealed both agreement with MF [27–30] and deviations from the universally predicted exponents [32,33]. More specifically, we recently reported that lattice type (fcc versus bcc) can affect the dynamics of avalanches quite distinctly, where average shape functions seem to deviate away from universal MF exponents in a bcc Nb microcrystal [33]. Based on this insight, we became increasingly interested in identifying material parameters or microstructural details that can underscore the nonuniversal dislocation avalanche dynamics, which is the main objective of this paper.

In this particular contribution, we expand our experimental insights into how the average dynamics of dislocation avalanches (slip events) behaves statistically when the crystal orientation is varied, or when one particular orientation is cold-rolled prior to assessing the avalanche dynamics. We find that both orientation and initial defect density of the crystals affect the average shape profile of the traced avalanches, suggesting that a very material-specific and thus nonuniversal process is taking place.

This article begins in Section 2 with outlining some subtle aspects of the data analysis and experimental features, which is shown to be crucial when evaluating the time-resolved traces of spatio-temporal avalanche dynamics. While Section 2 is long in comparison to the results section, we emphasize that the key findings of this article focus on orientation and predeformation effects on the avalanche shape functions. However, given the importance of subtleties in the denoising methods used when investigating velocity profiles, Section 2 is intended to give a solid foundation for the subsequently displayed results. Section 3 presents and discusses the results obtained from deformation experiments on Au microcrystals with a loading axis oriented along ⟨123⟩, ⟨011⟩, ⟨111⟩, and ⟨001⟩, respectively. We specifically pay attention to the velocity-profile shapes of differently oriented microcrystals, and also how these change in response to predeformation of the as-received bulk crystals. Our main insights are summarized in Section 4.

2 Experimental

2.1 Samples and experimental technique

The samples used in this study were cylindrical Au microcrystals with nominally 2 μm diameter and 6 μm height created by annular focused ion beam milling from bulk single crystals of several orientations. The orientations used were ⟨123⟩, ⟨011⟩, ⟨111⟩, and ⟨001⟩. To examine the effects of predeformation, the ⟨011⟩-oriented crystal was cut into multiple sections, with one being left as-grown, one rolled to a 30% reduction in thickness, and one rolled to a 75% reduction in thickness, followed by grinding/polishing and etching to produce a generally flat surface unaffected by deformation from polishing. The other crystals were all used in the as-grown state and are of equivalent origin as the Au crystals in our previous studies [31–33].

The microcrystals were compressed using a TI-950 Triboindenter with Performech® controller equipped with a flat punch tip under closed-loop displacement control. The used load function had a nominal displacement rate of 60 nm/s and data acquisition rate (DAR) of 16 kHz. All microcrystals were compressed to an engineering strain of 20–25%, with 9–14 microcrystals tested per data set. Details on the experimental approach can also be found in reference [33].

2.2 Wiener filtering and event extraction

The raw displacement–time data acquired from the nanoindenter is generally noisy due to the extreme sensitivity of the system, with typically subnanometer variance. In addition to noise due to the system sensitivity, the requirement of high DAR in order to properly trace the rapid slip events prevents us from averaging across longer time periods to reduce noise in the raw data, an otherwise generally effective method.

As we are analyzing the velocity, i.e., the time derivative of the displacement, it is important that this noise is minimized by filtering to ensure that it is not excessively amplified while taking the derivative. Previous work used a simple low-pass finite impulse response (FIR) filter to smooth the raw displacement data [33], which was reasonably effective due to the noise components being dominant at higher frequencies. However, more optimal filtering was desired. Wiener filtering, a frequency-domain filter based on the estimated signal-to-noise ratio at each frequency, had previously been used successfully for smoothing of event profiles in Barkhausen noise [34], so this was chosen as the new smoothing method.

Wiener filtering was implemented following the method outlined in *Numerical Recipes* (Chap. 13.3) [35]. The full displacement–time trace for a given test was taken as the raw data, with Matlab's implementation of the fast Fourier transform (FFT) function used to transform it into the frequency domain. This gives the corrupted frequency-domain signal $C(f)$. The squared complex modulus $|C(f)|^2$ gives an estimate of the power spectral density (PSD) of the data. In the presence of noise, this is approximately the sum of the PSD of the signal S and the noise N, i.e., $|C(f)|^2 \approx |S(f)|^2 + |N(f)|^2$ [35]. The Wiener filter coefficients $\phi(f)$ are calculated as $\phi(f) = |S(f)|^2/(|S(f)|^2 + |N(f)|^2)$. We thus need to obtain values of $|S(f)|^2$ and $|N(f)|^2$, which are estimated as smooth functions of frequency.

Figure 1 shows the PSD estimate of a zero-drive-rate test in elastic contact with one of the microcrystal samples. Note that this single-sided PSD does not go all the way to the nominal Nyquist frequency of 8 kHz for a DAR of 16 kHz. This is due to a feature of how the used Performech® controller acquires data, where it polls the transducer at a rate of 78 kHz, and then averages across an integer number of internal data points to produce the requested DAR as external output. This causes the

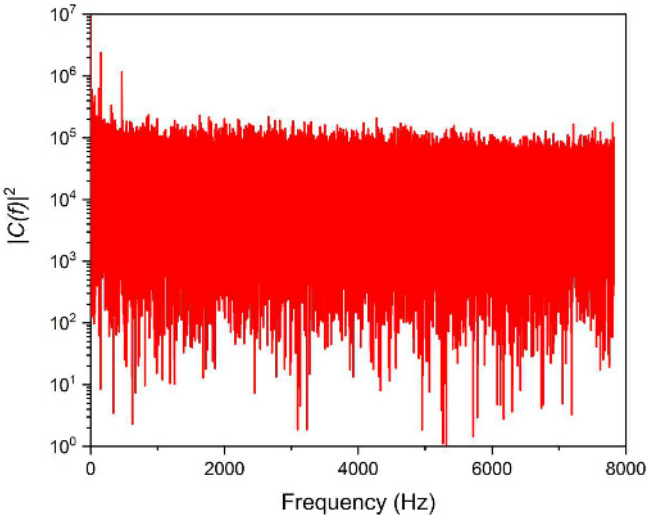

Fig. 1. Single-sided PSD of depth–time data from a stationary noise test in elastic contact with an ⟨001⟩-oriented sample.

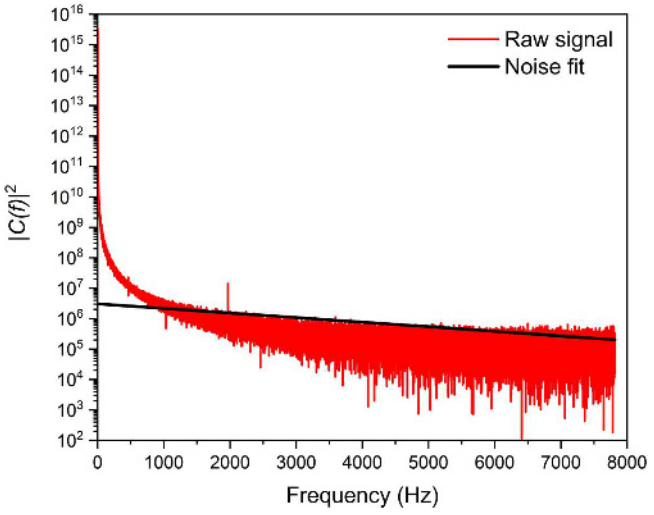

Fig. 2. Single-sided PSD of depth-time data from a microcrystal sample test with noise fit.

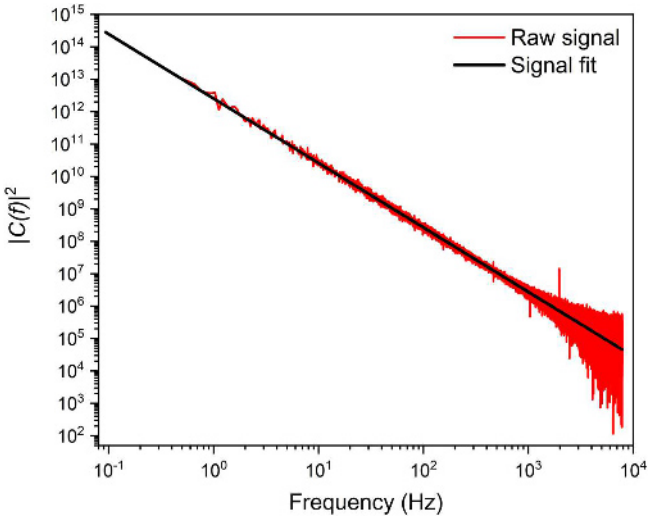

Fig. 3. Single-sided PSD of depth–time data from the same microcrystal sample test shown in Figure 2 with signal fit.

available DARs to be quantized when high rates are desired. For this work, the nominal DAR of 16 kHz results in an actual DAR of $78/5 = 15.6$ kHz.

In such a stationary noise test, the true signal component is expected to be zero, which is exemplified in Figure 1 and describes the behavior of $|N(f)|^2$ generally observed in our tests. The noise is very close to "white" noise, i.e., constant power at all frequencies, with the subtle characteristic of a linear slope visible in the data. This motivates the use of an exponential function fitted to the top of the noise envelope as the smooth model of $|N(f)|^2$, i.e., a straight line on a semi-logarithmic plot.

Figure 2 shows this model fitted to the PSD of one of the tested ⟨111⟩-oriented microcrystals. The frequency range used to fit $|N(f)|^2$ for all tests in this work was $N_f/4$ to N_f, where N_f is the Nyquist frequency, i.e., the maximum frequency displayed on the single-sided PSD plot. It is easily visible that at low frequencies the raw signal PSD rises well above the extrapolated noise floor. This is consistent with the expected behavior, given the significantly linear (i.e., low-frequency) displacement–time behavior of the displacement-controlled tests.

Having obtained our model of $|N(f)|^2$ as a smooth function of frequency, we now model the raw signal PSD at low frequencies as a smooth function in order to calculate $|S(f)|^2 \approx |C(f)|^2 - |N(f)|^2$. If the raw PSD is plotted on a log–log scale, it becomes clear that at low frequencies the PSD scales as a power-law with frequency, i.e., follows a straight line on the log–log plot. Figure 3 shows the PSD of the same test shown in Figure 2, now on a log–log scale with the fitted power-law signal model. The frequency range used to fit $|C(f)|^2$ for all tests in this work was 0 to $N_f/4$.

Having obtained these smooth models, we can now calculate $\phi(f) = (|C(f)|^2 - |N(f)|^2)/|C(f)|^2$, approximately equivalent to the original formula of $\phi(f) = |S(f)|^2/(|S(f)|^2 + |N(f)|^2)$. At any frequency where the filter coefficient would be less than zero (i.e., where the noise model is greater than the signal model), it is set to zero. The filter coefficients are calculated in a range of frequencies from 0 to N_f. The full set of coefficients is symmetric about the Nyquist frequency, so this first section is flipped and appended to itself (matching the frequency ordering used in Matlab's implementation of the FFT). Note that neither of the smooth models can be evaluated at $f = 0$. At that frequency the filter coefficient is directly set to 1, as the models imply that the signal should be highest there and the noise should be negligible relative to the signal.

To calculate the smoothed depth–time data, we multiply the initial frequency-domain signal values $C(f)$ by the corresponding filter values $\phi(f)$ at each frequency and take the inverse Fourier transform of the result. This gives a time-domain signal, typically with some small imaginary components. These imaginary components are dropped, although they serve as a sanity check for the performance

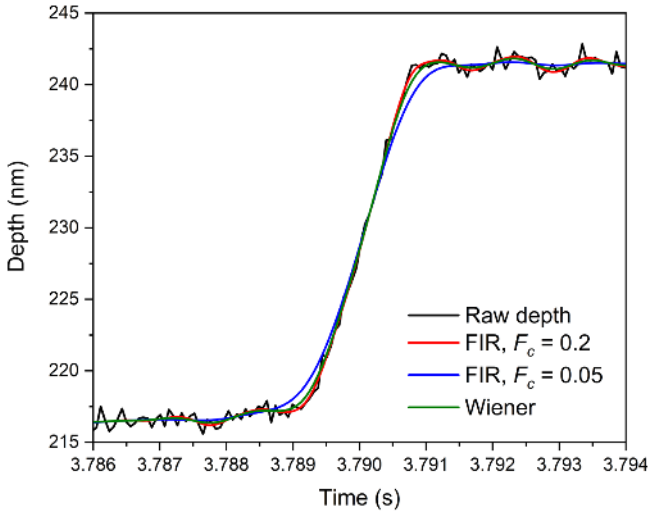

Fig. 4. Raw versus smoothed depth–time data during a slip event using Wiener filtering and FIR filtering with a cutoff frequency F_c of either 0.2 or 0.05.

of the filter – if they are too large, the filter is not performing well. Typical values in these tests are for all imaginary components of the filtered time-domain signal to be under a magnitude of 10^{-4}. Figure 4 compares a section of raw depth–time data with the smoothed data from a deforming Au⟨111⟩ microcrystal, using both the Wiener filtering method and denoising via a FIR filter, the latter of which will be addressed later in this manuscript. It is noted that the variations between the filtering methods are not significantly apparent from Figure 4, but we will later show how strong differences emerge when constructing the velocity–time data via a derivative.

Roughly 60 data points must be removed from both the beginning and the end of the smoothed data set due to the presence of spurious filtering-induced oscillations (edge effects). Since this smoothing is done to the entire curve at once, the data to be smoothed can be selected to ensure that the removed data points are not in important parts of the displacement–time curve. The longest possible sample is best, as an increased number of data points improve the frequency resolution of the FFT. However, it is important to exclude the "initial contact" and "final unloading" sections of the displacement–time curve, as making or breaking elastic contact of the tip with the microcrystal sample tends to generate large-amplitude (but low-force) displacement oscillations that are not present during the actual test and which can interfere with the filter calculations if included.

While this filtering method works excellently for the data sets used here and could theoretically be applied to any similar data set, it should be noted that there are conditions where it can perform poorly. The DAR must be high enough to ensure that there is a significant portion of the raw depth–time PSD that is dominated by the high-frequency noise background, with minimal signal. Similarly, if the drive rate is increased for a given DAR, for sufficiently high rates the signal component will be significant at frequencies approaching the Nyquist frequency, preventing an accurate estimate of the noise threshold in that experiment and reducing the effectiveness of the filter. In such cases, an alternate filtering method such as wavelet-based filtering or the previously used FIR filtering with manually determined parameters would likely have better performance.

Having produced the smoothed displacement–time data using Wiener filtering, the event velocity–time profiles, event extents, and other event parameters are calculated from the smoothed data as described in reference [33].

2.3 Frequency analysis of indenter system

During previous research [33], the question was raised as to whether the mechanical resonances of the indenter system (previously shown to behave as a damped harmonic oscillator [31]) might interfere with the behavior of intermittent flow via oscillations induced by the sudden acceleration(s) occurring during a given slip event.

To investigate this possibility, we used Welch's method to obtain PSD estimates of velocity–time data from several different test conditions. The velocity–time data was calculated directly from the raw displacement–time data using a two-point difference method to eliminate any effect of data filtering. The velocity was examined rather than the time because this amplifies any potential resonance effects that are present. This analysis method follows the technique described in the thesis of McFaul [36]. Performing the same analysis on the raw displacement–time data shows the resonance peaks less distinctly, or not at all. All tests had a nominal DAR of 16 kHz. As specified in the legend of Figure 5, some tests were conducted in displacement control, while others were in open-loop control (no feedback). The "air indent" test was conducted with the transducer tip out of contact with the sample, while the "Au⟨001⟩" tests were conducted in contact with a microcrystal sample of the specified orientation. The noise tests had a nominally zero drive rate, while the sample tests had a finite drive rate (60 nm/s for displacement control, 50 μN/s of electrostatically applied force without feedback corrections for open-loop control).

The PSD data shown in Figure 5 exists for frequencies up to the Nyquist frequency, but the curves become indistinguishable above a frequency of 1200 Hz due to noise amplification in the unfiltered velocity. Here, we focus on the lower frequency region where interesting differences are seen. In the air indent noise test, a broadened oscillation peak is seen in Figure 5a (with the PSD rising above that of the in-contact noise test) near or slightly above ∼140 Hz, which is the mechanical resonance frequency of the transducer by itself [31]. However, this peak is not seen in the other test conditions, which are all in elastic contact with a microcrystal sample. While in contact, the transducer is elastically coupled to the sample, which is much stiffer than the indenter support springs. The stiffness values are ∼360 N/m for the support springs and $\sim 1.0 \times 10^4$ N/m for the microcrystal sample, with the former from reference [31] and the latter calculated from the force/displacement slope of elastic unloading curves. Thus, in the elastically coupled system, the stiffness is dominated by the stiffness of the

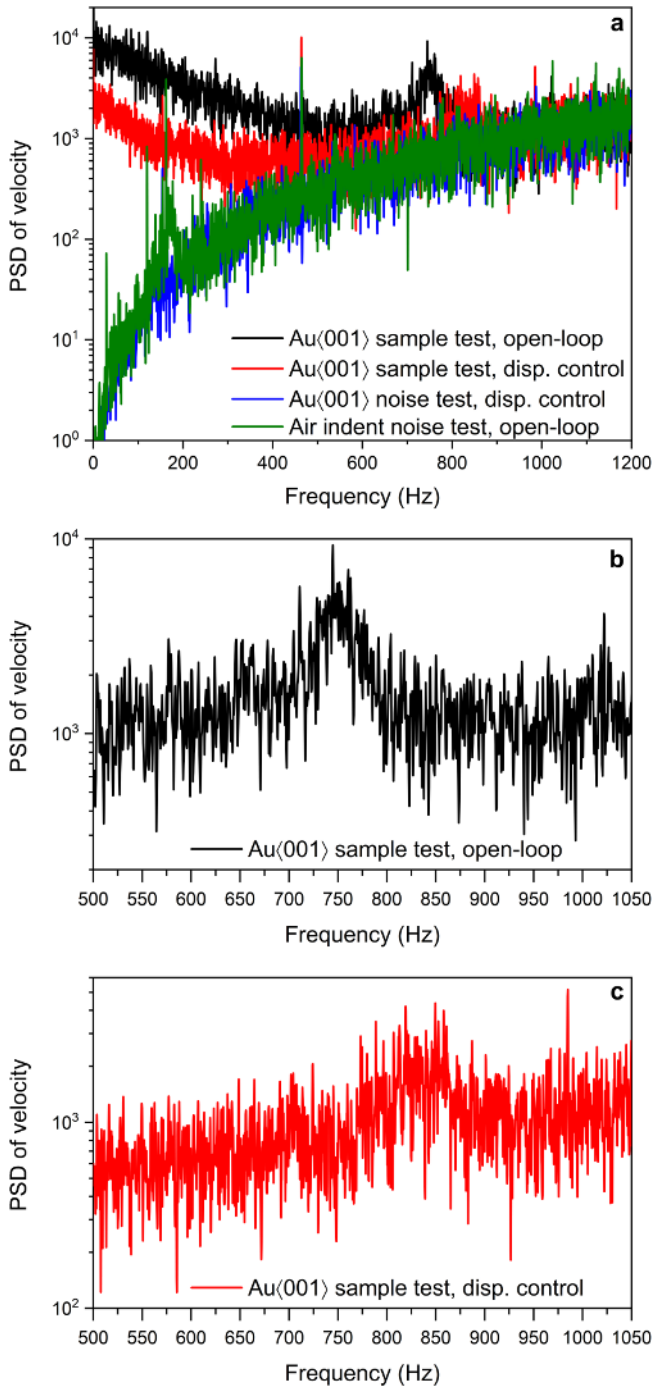

Fig. 5. (a) Unfiltered velocity PSDs in various test conditions. (b) and (c) Zoomed views of part (a). See text for details.

microcrystal. Similarly, the mobile mass of the transducer is 0.445 g, dominating the mass of the coupled system. In both the transducer and the sample, the damping is minimal, resulting in a calculated resonance frequency $2\pi\omega_0 = \sqrt{K/m}$ of ∼750 Hz for the coupled system. In the open-loop sample test, we do in fact find a broadened resonance peak at this frequency, as shown in Figure 5b. For the in-contact noise test no peak is seen, presumably because no major accelerations were present to induce harmonic oscillation, while in the sample tests almost impact-like accelerations occur as the intermittent flow starts and stops.

Importantly, in the displacement-controlled sample test, this peak is broader, relatively weaker (with the peak mostly visible in the locally increased maximum amplitude of the fluctuations), and shifted to slightly higher frequencies (∼775–875 Hz), as shown in Figure 5c. This implies that any mechanical resonance effects will be diminished in displacement-controlled tests (such as those used in this paper) relative to the open-loop case, if they are present. For a more detailed analysis of the open-loop case, see [37].

There is also a narrow peak appearing near a frequency of 465 Hz. This appears to be an effect from the measurement electronics, as the peak is present in both physical test conditions and both control modes, which is evidence against a mechanical or control-mode-based resonance. In Figures 2 and 3, a similar peak is visible around 2 kHz. This peak is not analyzed further, as it is in the frequency range that is entirely removed by the Wiener filtering. The ∼465 Hz peak is also visible in Figures 2 and 3 on close inspection, but its amplitude is low relative to the strong signal component, so any effects are assumed to be minimal.

3 Results and discussion

3.1 Microcrystal flow stress and strain hardening

Depending on orientation, the force–displacement curves produced from the microcrystal tests show a very reproducible trend of apparent hardening with strain. Figure 6a shows an example force–displacement curve from a test on a ⟨111⟩-oriented Au microcrystal, that being one of the orientations with a distinct apparent hardening slope.

However, the force–displacement data by itself is not directly comparable between orientations, due to the Schmid-factor effect on the resolved shear stress and shear strain. In addition, there is noticeable sample-to-sample variance between the flow curves of the microcrystals within a given sample set (a well-established trait of micro-compression testing [15,38,39]). To account for these effects and to give a more accurate overview of the stress–strain behavior of the different microcrystal sample types, Figure 6b shows a resolved shear-stress versus resolved shear-strain plot averaged across all samples of each type (9–14 samples per data set, see Sect. 2.1). The pristine crystals all show an initial flow stress of ∼32 MPa, significantly higher than the bulk single-crystal critical resolved shear-stress of 0.9 MPa [40] due to the size effect on strength [15].

The predeformed ⟨011⟩-oriented samples show very little apparent hardening during deformation of the microcrystals, similar to the pristine ⟨011⟩-oriented samples (which reach a "steady-state" flow stress almost immediately after deformation begins). However, the microcrystals made from the predeformed bulk material do show a significant effect of the increased initial dislocation density on the steady-state flow stress, increasing from

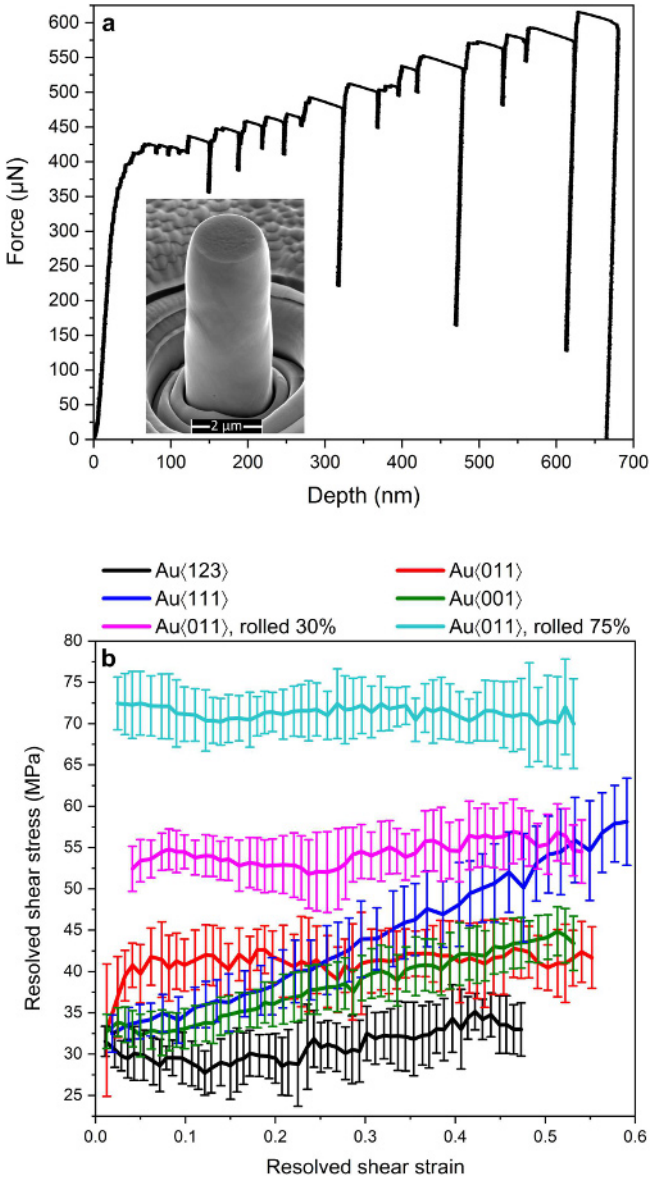

Fig. 6. (a) Force–displacement plot from an Au⟨111⟩ microcrystal test showing strain hardening, with inset showing a deformed Au⟨111⟩ sample. (b) Plot of mean resolved shear stress versus resolved shear strain for all sample sets used in this work.

∼41 MPa with no rolling to ∼54 MPa at 30% reduction and ∼71 MPa at 75% reduction. The obtained numbers of the predeformed orientation do not quite follow a trend according to Taylor hardening, as there the increase in strength is proportional to the square root of the dislocation density, with the latter generally being expected to increase much more rapidly at low deformations [41]. This can potentially be rationalized using a hardening model proposed by El-Awady, which expresses the strength as a sum of a forest hardening contribution and a source strengthening contribution [42]. In this model, below a size-dependent critical dislocation density, the strength no longer follows the bulk trend of $\sigma \propto A_\rho^{0.5}$ (where A is an empirical constant), instead staying roughly constant for a range of approximately two orders of magnitude in ρ. The scaling is predicted to change further for even lower values of ρ, but this requires dislocation densities so low that they are likely experimentally inaccessible. If the initial dislocation density in the here tested as-grown crystal was in this critical region, the increase in microcrystal strength from the initial (larger) jump in dislocation density could plausibly be lower than from the following (smaller) jump in dislocation density. Such a hypothesis could be corroborated in more quantitative detail by direct TEM investigation of the dislocation density in the bulk ⟨011⟩-oriented crystals and/or the deformed microcrystal samples themselves.

It can also be seen in Figure 6b that of the two high-symmetry orientations having a well-defined, non-negligible apparent strain-hardening rate, it is the ⟨111⟩-oriented samples that have the highest strength increase per unit strain. This is fairly consistent with results from bulk single-crystal testing [43,44], with the high initial hardening rates in the ⟨111⟩ or ⟨001⟩ orientations generally attributed to the continuous formation of sessile dislocations by reactions between glide dislocations on intersecting active slip systems with the appropriate relative orientations. In other crystal orientations, such consistently high hardening rates are generally not seen until the end of stage I "easy glide" deformation, which can be significantly extended in small-scale samples [45].

3.2 Sensitivity of size–velocity scaling to filtering

Force–displacement data as shown in Figure 6a is analyzed with respect to the time-resolved velocity profile of each individual force–displacement discontinuity. In any discussion of peak velocities or velocity profiles during intermittent flow, it is important to note that these quantities can be sensitive to the precise filter details. With FIR filtering, it is up to the user to define the filter parameters, particularly the cutoff frequency F_c (see Ref. [33]). With Wiener filtering, optimal parameters are automatically calculated based on the measured characteristics of the data, so it might be expected to be less subjective.

An easy illustration of this sensitivity is a plot of measured event size versus measured peak velocity for different filters on the same raw data. All three data sets displayed in Figure 7 use the raw Au⟨001⟩ data that was used in reference [33], and FIR filtering with $F_c = 0.2$ was the filter used there. While the event sizes are only negligibly affected, it can be easily seen that using Wiener filtering results in a noticeable change in the size–velocity scaling, particularly for low-size/low-velocity events where the signal-to-noise ratio of the velocity measurement is expected to be lowest. The primary effect stems from changing the effective cutoff frequency F_c, rather than from changing the filter method, as using FIR filtering with a reduced $F_c = 0.1$ produces essentially identical results when compared to Wiener filtering of this data set.

It appears that the cutoff frequency used for the Au data in reference [33] is not in precise agreement with the Wiener filtering methods, allowing more noise to pass

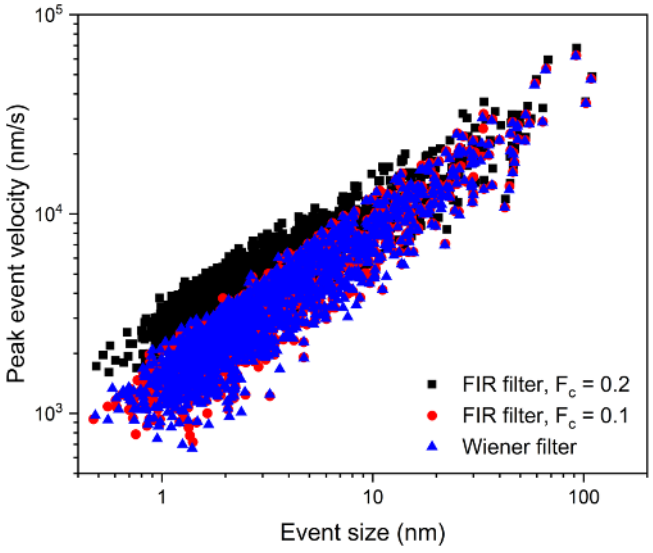

Fig. 7. Event size/peak velocity values of individual events in the same Au⟨001⟩ raw data using different filter characteristics.

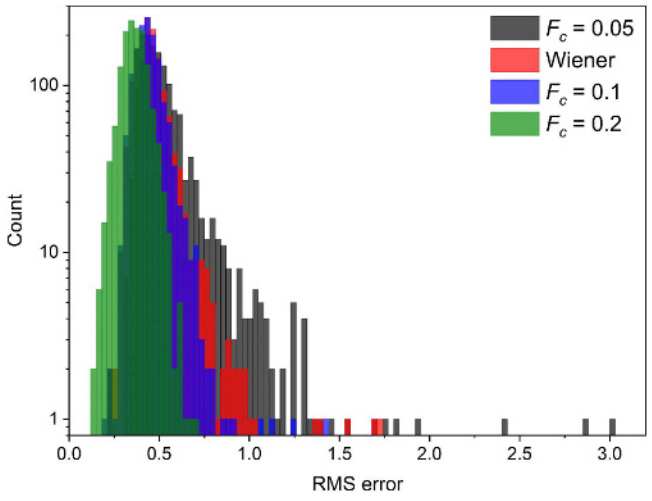

Fig. 8. Histogram of the RMS error within individual events, using Wiener filtering and FIR filtering with different cutoff frequencies.

through into the smoothed displacement data. While it may be tempting to decrease F_c further to continue reducing noise in the data, this will increase the degree to which the smoothed depth–time data pulls away from the raw data (visible in Fig. 4). If we track the distribution of root-mean-square (RMS) error values between raw and smoothed depth data within individual events, we find that decreasing F_c from 0.1 to 0.05 increases the average RMS error (averaged across all events) from 0.447 to 0.538 nm, the skewness of the RMS error distribution from 2.56 to 4.72, and the kurtosis from 20.5 to 42.0. These values are numerically expressing the differences in the distributions seen in Figure 8. Given that the Wiener filter is based on a quantitative estimate of the signal-to-noise ratio, we choose to use it as a limit for the "harshness" of the smoothing, and therefore do not consider $F_c = 0.05$ further.

While the difference in power-law scaling between peak velocity and event size is noticeable, it is not massive relative to the calculated variance of the scaling exponents. The value of the size–velocity scaling exponent found in reference [33] (with 95% confidence interval) was 0.656 ± 0.076, while the value found using the Wiener filtering is 0.738 ± 0.077. Thus, the two values are only barely outside of each other's confidence intervals. However, it should be noted that the Wiener-filtering value of the scaling exponent is even further away from the MFT-predicted value of 0.5 [23,46].

3.3 Size-binned velocity profiles and scaling collapse

As was also described in reference [33], MFT predicts that averaging event velocity profiles across narrow bins of event size should produce self-similar mean profiles, collapsing onto each other when rescaled with respect to the central size value of each bin. Interestingly, it was found that while the MFT-predicted scaling value of $S^{-0.5}$ (where S is the central bin size) produced a good collapse

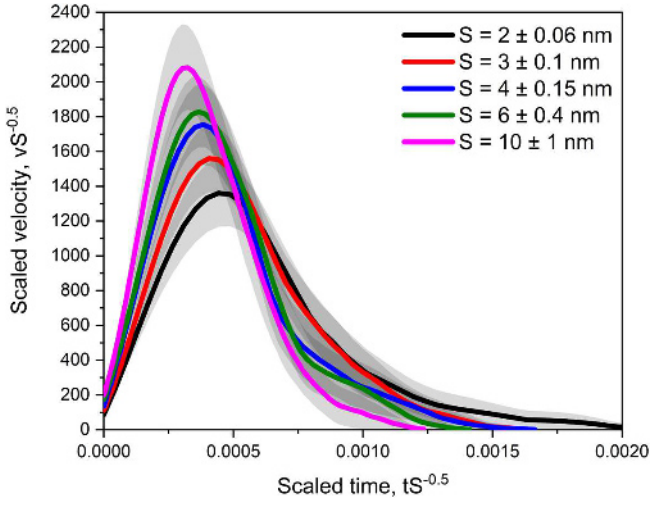

Fig. 9. Size-binned mean velocity profiles in Au⟨001⟩ microcrystals with time and velocity scaled by a factor of $S^{-0.5}$, where S is the central bin size. Shaded areas are 95% confidence intervals for each curve. Note the lack of collapse (curves are not overlapping each other).

with FIR filtering and $F_c = 0.2$, Wiener filtering pushes the measured size–velocity scaling further away from an exponent of 0.5. As a consequence, a collapse with $S^{-0.5}$ no longer produces good agreement between the collapsed velocity profiles when using on the same raw Au⟨011⟩ data, which is shown in Figure 9. This filtering-induced shift appears to be unrelated to the potential mechanical resonance effects discussed in Section 2.3.

However, the velocity profiles can, in fact, still be shown to be self-similar; it is the scaling factor for the collapse that has changed. Empirically, as stated in Section 3.2, we found that under the Wiener filtering, the peak velocities scale with event size as $V_{max} \sim S^{0.738 \pm 0.077}$. As a good approximation, we therefore alter the scaling factor for

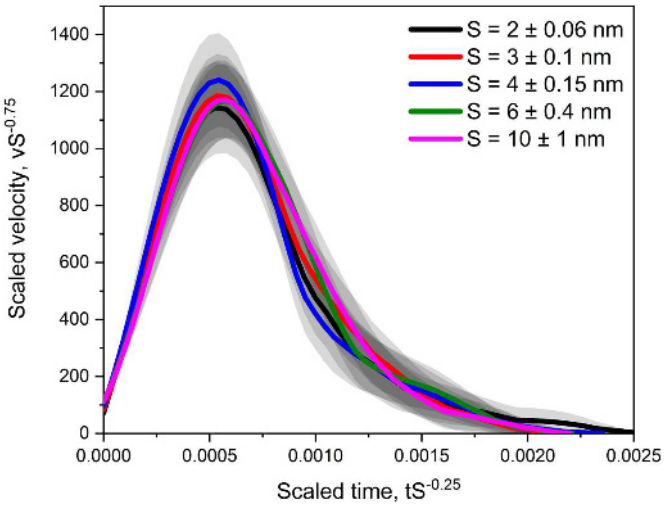

Fig. 10. Size-binned mean velocity profiles in Au⟨001⟩ microcrystals with time scaled by a factor of $S^{-0.25}$ and velocity scaled by a factor of $S^{-0.75}$, where S is the central bin size. Shaded areas are 95% confidence intervals for each curve. Note the excellent collapse (curves are overlapping each other).

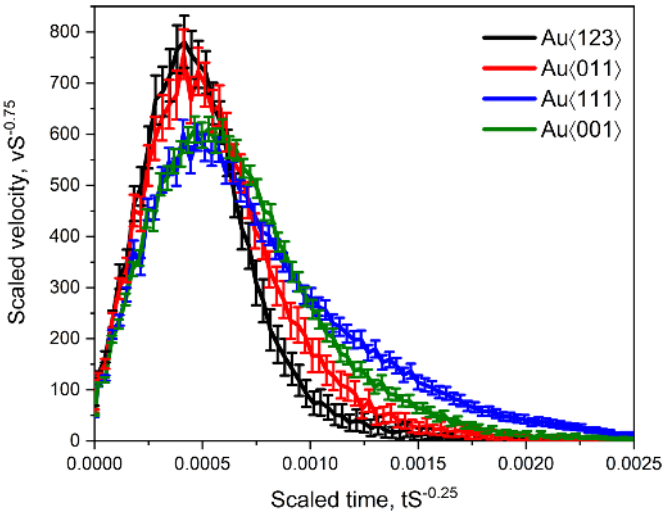

Fig. 11. Size-integrated mean velocity profiles versus orientation in Au microcrystals.

the velocity to $S^{-0.75}$ intended to rescale the peak velocities in each size bin to the same value. The scaling factor for the time also needs to be altered. The plot of event size versus duration (not shown) has less consistent scaling than the plot of event size versus velocity, and it is thus not ideal to calculate the exponent from the size–duration scaling data. Instead, we empirically find that the *average* velocity during an event, calculated as $S/\Delta t$, has a strong linear correlation with the peak event velocity (linear regression $R^2 > 0.97$ for all data sets used in this work). Given that linear correlation, if the peak velocity scales with size as S^α, the duration Δt should scale with size as $S/S^\alpha \propto \Delta t \propto S^{1-\alpha}$, so we estimate that the duration should scale with event size as $\Delta t \sim S^{0.25}$, and therefore define the new time rescaling factor as $S^{-0.25}$. Figure 10 shows the same size-binned mean velocity profiles with the empirical rescaling factors; it can easily be seen that they now collapse very well onto each other.

3.4 Size-integrated velocity profiles and effects of orientation

While the size-binning method can produce interesting results, it is limited in that it requires the collection of a very large amount of data to be feasible. Ideally, each bin would both be as narrow as possible to ensure that all events in the bin are very close to each other in size and contain as many events as possible to ensure that the averaged profiles are reliable and not strongly affected by outliers. Particularly for larger events, this is experimentally difficult to accomplish due to the increasing rarity of events as the desired size increases [16,18,47,48]. This can be seen in Figures 9 and 10, where the specified size bins become significantly wider as the central size increases (each bin radius was chosen to encompass at least 40 events).

Table 1. Fit parameters for the data shown in Figure 11.

Data set	A	B	C	R^2
Au⟨123⟩	2.70×10^6	1.36×10^8	2.52 ± 0.15	0.992
Au⟨011⟩	2.68×10^6	1.97×10^6	1.96 ± 0.11	0.992
Au⟨111⟩	2.65×10^6	1.45×10^4	1.28 ± 0.06	0.991
Au⟨001⟩	2.07×10^6	6.24×10^5	1.83 ± 0.07	0.994

An alternate method of calculating averaged velocity profiles is to rescale the velocity profile of *each individual event* by the time and velocity scaling factors, and then average them together, in contrast to the size-binned method where individual profiles are averaged together and then rescaled. This allows for every event within a large size range to contribute to the averaged profile, with the combination of events across a large, continuous size range suggesting the name of "size-integrated" velocity profile.

In Figure 11, we use the $S^{-0.25}$ time-scaling factor and $S^{-0.75}$ velocity-scaling factor established in Section 3.3 to produce size-integrated velocity profiles across an event size range of 1.5–15 nm for all tested Au crystal orientations $-\langle 123\rangle$, $\langle 011\rangle$, $\langle 111\rangle$, and $\langle 001\rangle$. It should be noted that if the MFT-predicted scaling factor of $S^{-0.5}$ is used instead of the empirically adjusted scaling factors, the observed trends are qualitatively the same.

As the crystal symmetry increases, there is clearly a general trend of decreased peak velocity and extended decay time. In order to quantify this decay, the mean profiles are fitted using a function of the form $Ax\exp(-Bx^c)$, with A, B, and C being fit parameters. The MFT-predicted shape function for the velocity profiles had the decay exponent C fixed at 2 [46,49,50], but we found it necessary to allow it to vary freely in order to obtain good fits to the observed profiles. This was articulated in reference [33], with the important difference that the Au⟨001⟩ size-binned mean velocity profiles can provide good agreement with the MFT value of $C = 2$ in

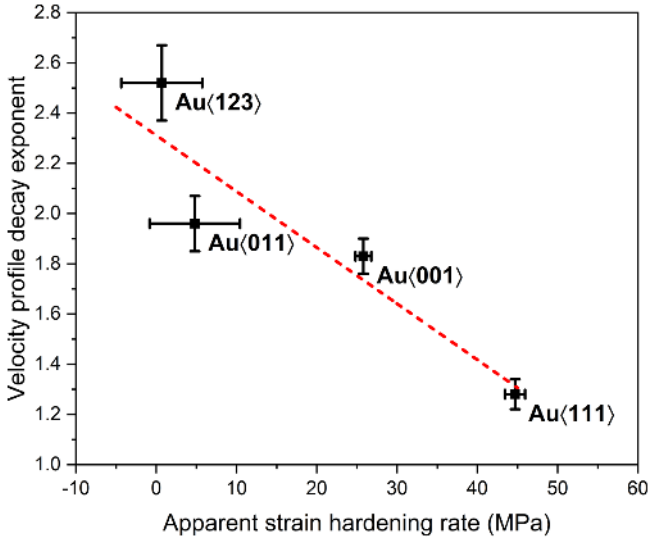

Fig. 12. Apparent strain-hardening rate versus decay exponent C for different orientations of Au microcrystals, with linear fit.

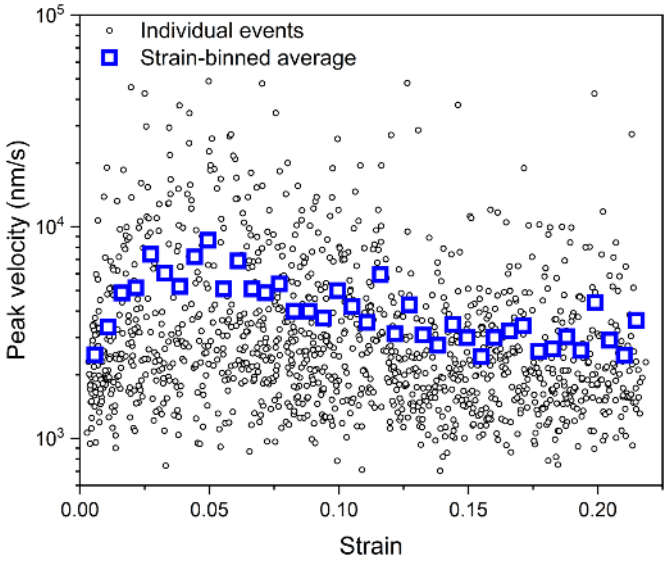

Fig. 13. Peak event velocity versus engineering strain in Au⟨111⟩ microcrystal samples at the time of the event.

closed-loop displacement-controlled tests when the FIR filter with $F_c = 0.2$ is used. It thus appears that the precise details of filtering methods can significantly affect conclusions when comparisons between experiments and theory are made. Table 1 gives a summary of the results of the nonlinear fits to the data in Figure 11.

Note that it is not the four-fold Au⟨001⟩ orientation that has the most extended velocity decay in Figure 11, but rather the three-fold Au⟨111⟩ orientation. This is consistent with the fact that the Au⟨111⟩ orientation had the highest overall apparent strain-hardening rate in these microcrystal tests, and that the decay exponent C was found to have a good linear relationship with the overall apparent hardening rate (see Fig. 12). The estimates of the apparent hardening rate are taken from the data shown in Figure 6b. It is worth noting that in the two high-symmetry orientations, out of the slip systems activated according to Schmid-factor calculations, each active slip direction can be associated with *two* slip planes, i.e., it is possible for a dislocation to cross-slip from one active slip plane to another one. In the lower symmetry orientations, each active slip direction is associated with a single active slip plane, and cross-slip of an active dislocation to another plane would cause said dislocation or dislocation segment to experience a strongly reduced resolved shear-stress and therefore restricted motion.

Our current hypothesis is that the increased propensity for active cross-slip of dislocations in the high-symmetry orientations leads to the extended velocity relaxation seen in the mean velocity profiles. In lower symmetry orientations, cross-slip can cause cessation of dislocation movement and thus the halting of the event, while in higher symmetry orientations the dislocations remain active but may take an increasingly lengthy and convoluted path to their final destination, potentially increasing the overall event duration and thus extending the velocity relaxation as seen in the mean profiles.

Following earlier reports on strengthening of microcrystals [51–53], we expect that a significant evolution of the dislocation structure, as qualitatively expressed above, occurs prior to the point at which large amounts of strain are generated (breakaway stress). This means that the avalanche dynamics studied here can be regarded as occurring in an environment of crudely approximated network constancy, being in line with references [51–53] and also the fact that the spatiotemporal dynamics traced here are not seen to vary noticeably with plastic strain in the microcrystals (see Fig. 13). The latter has been reported earlier [27]. It is emphasized that this working assumption only has validity if the apparent strain-hardening slope evaluated earlier is not understood classically in the sense that this strength increase per unit strain increment originates from a continuously increasing network entanglement. Instead, we consider the limited source statistics and its changes with strain as the determining factor behind the dependence displayed in Figure 12.

As a toy model, we can therefore consider the activation of single-arm sources [54,55] that mediate the growth of a given event via a repeated operation. Under the assumption of slip being primarily driven by rotation of single-arm sources, the number of immobile forest dislocations that must be intersected per rotation is directly related to the overall dislocation density in the crystal. Consequently, for one full rotation of a single armed source, one Burgers vector of slip is generated, but for different dislocation densities a larger number of pinning points is expected to decrease the mean deposition rate of Burgers vectors per unit time, which is the property contained in our average and peak velocity data. If each intersection event delays the motion of the dislocation by some finite time on average, then increasing the dislocation density would be expected to increase the duration of a slip event relative to its size and therefore extend the velocity relaxation of the scaled mean profile.

Table 2. Fit parameters for the data shown in Figure 14. The label "red," in the most left column refers to thickness "reduction."

Data set	A	B	C	R^2
0% red	2.68×10^6	1.97×10^6	1.96 ± 0.11	0.992
30% red	2.51×10^6	3.44×10^5	1.72 ± 0.08	0.992
75% red	2.09×10^6	3.08×10^4	1.39 ± 0.05	0.994

It should thus be possible to qualitatively examine this by predeforming the bulk crystals to increase their initial dislocation density. The hypothesis is that the average shape function should exhibit a reduction in peak velocity and display a longer velocity decay due to predeformation, which will be tested in the following section.

3.5 Effects of predeformation on size-integrated velocity profiles

In order to investigate whether an increased density of immobile "forest" dislocations had any effect on the mean velocity profiles, two sections of the ⟨011⟩-oriented Au crystal were cold-rolled to a reduction in thickness of 30 and 75%, respectively. The mean velocity profiles of microcrystals produced from these bulk crystals are given in Figure 14. As with the effect of orientation, there is a clear decrease in peak velocity and extension of the velocity relaxation with increasing dislocation density, which supports our expectation based on the correlation and interpretation of the data captured in Figure 12. The decay exponent decreases from 1.96 ± 0.11 in the pristine state to 1.72 ± 0.08 after a 30% reduction, and decreases further to 1.39 ± 0.05 after a 75% reduction. Table 2 gives a summary of the results of the nonlinear fits to the data in Figure 14.

We find that there is a strong linear correlation between the decay exponent C and the peak velocity in each mean profile (as shown in the inset of Fig. 14). This is a nontrivial result, as mathematically the peak velocity is nonlinear in C, specifically scaling as $V_{\max} = Ae^{-1/C}(BC)^{-1/C}$ (the analytical solution for the curve maximum). Therefore, in order to produce this result, the data underlying the fitted curves must have been best fit by values of A and B that simultaneously changed in the manner required to produce a linear correlation of the peak velocity with C. Such a correlation is *not* found in the orientation-dependent mean profiles, as there is a significant difference between the decay exponent of the ⟨111⟩- and ⟨001⟩-oriented mean profiles but minimal difference between their peak velocities. It would be interesting to see if this correlation is consistent for further levels of predeformation in ⟨011⟩-oriented crystals, or if it exists for other orientations.

Given the distinct change in mean profile with increasing predeformation, we thus conclude that the density of dislocations (or of any other penetrable pinning points) after the breakaway stress will affect the fine details of the averaged spatiotemporally resolved slip dynamics. This translates into a material-specific picture of so-called avalanches and their dynamics in crystal plasticity. It is noted that such a scenario means that the evolution of the internal dislocation structure is insignificant in comparison to the structural state present at the moment when intermittency begins. This can only be regarded as a special feature for the here tested microcrystals, and we anticipate that a plastic strain dependence would emerge in bulk crystals, if one were able to resolve the here studied dynamics.

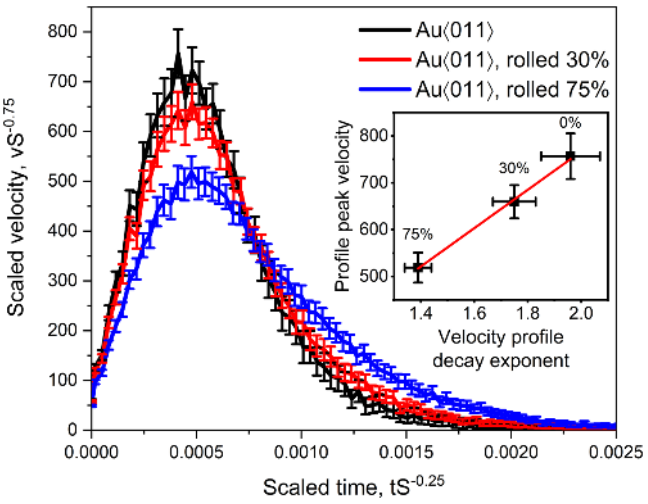

Fig. 14. Size-integrated mean velocity profiles versus predeformation in ⟨011⟩-oriented Au microcrystals. Inset shows the strong correlation (with the red line being a linear fit) between the decay exponent C and the peak value of the velocity for each level of rolling reduction.

4 Summary

Tracing experimentally the dynamics of collective dislocation rearrangements in gold microcrystals of various crystallographic orientations, or with different preexisting dislocation densities, reveals how average peak velocities and average shape functions yield systematic trends. This suggests to us that, similar as the non-trivial size-scaling exponent [56], the dynamics of dislocation avalanches (slip) is dependent on the microstructure present prior to the onset of intermittent flow of the tested gold crystals. In contrast, there is no evidence of a dependence on plastic strain accumulated during a deformation experiment, as the probed parameters do not, within the present fluctuations, display any noticeable change during intermittent flow, even when the apparent strain-hardening rates differ. Employing the established view of slip dominated by the operation of single armed sources in microcrystals, the results suggest that an increased density of pinning points (here forest dislocations) reduces the average peak velocity and also the velocity relaxation of slip. We finally note that even though we have shown how some of the fine details of the used data manipulation can affect the numerical results, their quantitative trends appear to be robust against such variations.

The authors thank L.W. McFaul, W.J. Wright, and K.A. Dahmen for fruitful discussions regarding mechanical

resonances and denoising of experimental data. This research was carried out in part in the Frederick Seitz Materials Research Laboratory Central Research Facilities, University of Illinois. R.M. is grateful for financial support by the NSF CAREER program (grant NSF DMR 1654065), and for start-up funds provided by the Department of Materials Science and Engineering at UIUC.

Author contribution statement

All experimental work was done by G. Sparks. Both authors contributed equally to interpreting the data, writing, and editing the paper.

References

1. J.P. Sethna, K.A. Dahmen, C.R. Myers, Nature **410**, 242 (2001)
2. J.P. Sethna, M.K. Bierbaum, K.A. Dahmen, C.P. Goodrich, J.R. Greer, L.X. Hayden, J.P. Kent-Dobias, E.D. Lee, D.B. Liarte, X. Ni, K.N. Quinn, A. Raju, D.Z. Rocklin, A. Shekhawat, S. Zapperi, Annu. Rev. Mater. Res. **47**, 217 (2017)
3. R. Becker, E. Orowan, Z. Phys. **79**, 566 (1932)
4. R.F. Tinder, J.P. Trzil, Acta Metall. **21**, 975 (1973)
5. J. Weiss, J.R. Grasso, J. Phys. Chem. B **101**, 6113 (1997)
6. M.C. Miguel, A. Vespignani, S. Zapperi, J. Weiss, J.R. Grasso, Nature **410**, 667 (2001)
7. A.J. Beaudoin, P.A. Shade, J.C. Schuren, T.J. Turner, C. Woodward, J.V. Bernier, S.F. Li, D.M. Dimiduk, P. Kenesei, J.S. Park, Phys. Rev. B **96**, (2017)
8. F. Chmelík, A. Ziegenbein, H. Neuhäuser, P. Lukáč, Mater. Sci. Eng. A **324**, 200 (2002)
9. F. Chmelík, F.B. Klose, H. Dierke, J. Šachl, H. Neuhäuser, P. Lukáč, Mater. Sci. Eng. A **462**, 53 (2007)
10. I.V. Shashkov, M.A. Lebyodkin, T.A. Lebedkina, Acta Mater. **60**, 6842 (2012)
11. T.A. Lebedkina, D.A. Zhemchuzhnikova, M.A. Lebyodkin, Phys. Rev. E **97**, 013001 (2018)
12. N. Kiesewetter, Scr. Metall. **8**, 249 (1974)
13. N. Kiesewetter, P. Schiller, Phys. Status Solidi A **38**, 569 (1976)
14. C.B. Scruby, H.N.G. Wadley, K. Rusbridge, D. Stockham-Jones, Metal Sci. **15**, 599 (1981)
15. M.D. Uchic, D.M. Dimiduk, J.N. Florando, W.D. Nix, Science **305**, 986 (2004)
16. F.F. Csikor, C. Motz, D. Weygand, M. Zaiser, S. Zapperi, Science **318**, 251 (2007)
17. R. Maass, P.M. Derlet, Acta Mater. **143**, 338 (2018)
18. D.M. Dimiduk, C. Woodward, R. Lesar, M.D. Uchic, Science **312**, 1188 (2006)
19. M.J. Alava, L. Laurson, S. Zapperi, Eur. Phys. J. Special Topics **223**, 2353 (2014)
20. E.K.H. Salje, K.A. Dahmen, Annu. Rev. Condens. Matter Phys. **5**, 233 (2014)
21. S. Papanikolaou, Y. Cui, N. Ghoniem, Model. Simul. Mat. Sci. Eng. **26**, 013001 (2018)
22. K.A. Dahmen, Y. Ben-Zion, J.T. Uhl, Phys. Rev. Lett. **102**, 175501 (2009)
23. M. LeBlanc, L. Angheluta, K. Dahmen, N. Goldenfeld, Phys. Rev. E **87**, 022126 (2013)
24. M.C. Miguel, A. Vespignani, M. Zaiser, S. Zapperi, Phys. Rev. Lett. **89**, 165501 (2002)
25. L. Laurson, M.C. Miguel, M.J. Alava, Phys. Rev. Lett. **105**, 015501 (2010)
26. P.D. Ispanovity, L. Laurson, M. Zaiser, I. Groma, S. Zapperi, M.J. Alava, Phys. Rev. Lett. **112**, 235501 (2014)
27. R. Maass, P.M. Derlet, J.R. Greer, Scr. Mater. **69**, 586 (2013)
28. R. Maass, P.M. Derlet, J.R. Greer, Small **11**, 341 (2015)
29. R. Maass, C.A. Volkert, P.M. Derlet, Scr. Mater. **102**, 27 (2015)
30. R. Maass, M. Wraith, J.T. Uhl, J.R. Greer, K.A. Dahmen, Phys. Rev. E **91**, 042403 (2015)
31. G. Sparks, P.S. Phani, U. Hangen, R. Maass, Acta Mater. **122**, 109 (2017)
32. Q. Rizzardi, G. Sparks, R. Maass, JOM **70**, 1088 (2018)
33. G. Sparks, R. Maass, Acta Mater. **152**, 86 (2018)
34. S. Papanikolaou, F. Bohn, R.L. Sommer, G. Durin, S. Zapperi, J.P. Sethna, Nat. Phys. **7**, 316 (2011)
35. W.H. Press, S.A. Teukolsky, W.T. Vetterling, B.P. Flannery, *Numerical Recipes 3rd Edition: The Art of Scientific Computing* (Cambridge University Press, Cambridge, 2007)
36. L.W. McFaul, Ph.D. thesis, University of Illinois at Urbana-Champaign, 2018
37. L.W. McFaul, G. Sparks, J. Sickle, J.T. Uhl, W.J. Wright, R. Maaß, K.A. Dahmen, manuscript under review
38. D.M. Dimiduk, M.D. Uchic, T.A. Parthasarathy, Acta Mater. **53**, 4065 (2005)
39. M.D. Uchic, D.M. Dimiduk, Mater. Sci. Eng. A **400**, 268 (2005)
40. S.G. Corcoran, R.J. Colton, E.T. Lilleodden, W.W. Gerberich, Phys. Rev. B **55**, R16057 (1997)
41. T.G.D. Sousa, V.L. Sordi, L.P. Brandão, Mater. Res. **21**, (2017)
42. J.A. El-Awady, Nat. Commun. **6**, 5926 (2015)
43. T. Takeuchi, Trans. Japan Inst. Metals **16**, 629 (1975)
44. L.M. Clarebrough, M.E. Hargreaves, Aust. J. Phys. **13**, 316 (1960)
45. L.M. Brown, Mater. Sci. Technol. **28**, 1209 (2014)
46. J. Antonaglia, W.J. Wright, X. Gu, R.R. Byer, T.C. Hufnagel, M. LeBlanc, J.T. Uhl, K.A. Dahmen, Phys. Rev. Lett. **112**, 155501 (2014)
47. K.S. Ng, A.H.W. Ngan, Acta Mater. **56**, 1712 (2008)
48. N. Friedman, A.T. Jennings, G. Tsekenis, J.Y. Kim, M. Tao, J.T. Uhl, J.R. Greer, K.A. Dahmen, Phys. Rev. Lett. **109**, 095507 (2012)
49. G. Durin, F. Bohn, M.A. Correa, R.L. Sommer, P. Le Doussal, K.J. Wiese, Phys. Rev. Lett. **117**, 087201 (2016)
50. A. Dobrinevski, P. Le Doussal, K.J. Wiese, Europhys. Lett. **108**, 66002 (2014)
51. D.M. Norfleet, D.M. Dimiduk, S.J. Polasik, M.D. Uchic, M.J. Mills, Acta Mater. **56**, 2988 (2008)
52. S.H. Oh, M. Legros, D. Kiener, G. Dehm, Nat. Mater. **8**, 95 (2009)
53. R. Maass, M.D. Uchic, Acta Mater. **60**, 1027 (2012)
54. S.I. Rao, D.M. Dimiduk, M. Tang, M.D. Uchic, T.A. Parthasarathy, C. Woodward, Philos. Mag. **87**, 4777 (2007)
55. S.I. Rao, D.M. Dimiduk, T.A. Parthasarathy, M.D. Uchic, M. Tang, C. Woodward, Acta Mater. **56**, 3245 (2008)
56. G. Sparks, R. Maaß, Phys. Rev. Mater. **2**, 120601 (2018)